AGU ADVANCING EARTH AND SPACE SCIENCES

Earth and Space Science

RESEARCH ARTICLE
10.1029/2024EA003540

Separation of Water Level Change From Atmospheric Artifacts Through Application of Independent Component Analysis to InSAR Time Series

Saoussen Belhadj-aissa[1], Marc Simard[1], Cathleen E. Jones[1], Talib Oliver-Cabrera[1], and Alexandra Christensen[1]

[1]Jet Propulsion Laboratory, California Institute of Technology, Pasadena, CA, USA

Key Points:

- Independent Component Analysis (ICA) is used to remove the wet troposphere noise in an InSAR-derived time series of water level change in wetlands
- In-situ data are used to identify components showing water level change and the other components used to generate tropospheric delay maps
- The filtered water level change values have improved accuracy based on measurements from water gauges located throughout the wetlands

Correspondence to:

S. Belhadj-aissa,
saoussen.belhadj.aissa@jpl.nasa.gov

Citation:

Belhadj-aissa, S., Simard, M., Jones, C. E., Oliver-Cabrera, T., & Christensen, A. (2024). Separation of water level change from atmospheric artifacts through application of independent component analysis to InSAR time series. *Earth and Space Science*, *11*, e2024EA003540. https://doi.org/10.1029/2024EA003540

Received 19 JAN 2024
Accepted 29 MAY 2024

Author Contributions:

Conceptualization: Saoussen Belhadj-aissa, Marc Simard, Cathleen E. Jones
Data curation: Talib Oliver-Cabrera, Alexandra Christensen
Formal analysis: Saoussen Belhadj-aissa
Investigation: Saoussen Belhadj-aissa, Marc Simard, Cathleen E. Jones, Talib Oliver-Cabrera, Alexandra Christensen
Methodology: Saoussen Belhadj-aissa
Resources: Marc Simard, Cathleen E. Jones, Talib Oliver-Cabrera, Alexandra Christensen
Supervision: Marc Simard, Cathleen E. Jones

Abstract In recent years, synthetic aperture radar (SAR) interferometry (InSAR) has emerged as a valuable tool for measuring water level change (WLC) to study hydrodynamic processes in coastal wetlands. However, the highly dynamic wet atmosphere conditions common in these areas have a significant impact on InSAR observations, producing errors in the derived values. Standard methods for estimating atmospheric noise in InSAR time series lack the spatial or temporal resolution needed to adequately correct for wet tropospheric delays. In this study, we utilize the Independent Component Analysis (ICA) signal decomposition technique to identify the likely WLC signal and eliminate atmospheric noise in a time series derived from rapid repeat measurements made with the L-band uninhabited aerial vehicle synthetic aperture radar airborne instrument. The method compares in-situ water level measurements with the independent components (IC) to identify the ICA components corresponding to WLC. The signal-to-noise ratio between the WLC after the ICA-based filtering and in situ water level gauges used for validation reaches 16 dB compared to an average of 2.6 dB before filtering. The excluded IC are used to generate maps showing a time series of likely atmospheric features. The identified features in the maps generally correspond to atmospheric features identifiable in Next Generation Weather Radar (NEXRAD) S-band ground weather radar reflectivity maps collected during the SAR acquisitions. The method is sufficiently general to be applied to any InSAR-derived surface displacement time series.

1. Introduction

Studying and monitoring coastal wetlands are essential for the conservation and sustainable management of these ecosystems, especially in the face of sediment starvation, climate change, and rising sea levels (Jankowski et al., 2017). Understanding the flow of water, sediment, and nutrients within wetlands provides insight into their overall functionality and aids in the early detection of hydrological imbalances that can impact their sustainability (Giosan et al., 2014). Coastal wetlands are shaped by hydrodynamic processes occurring at the interface between land and sea (Hopkinson et al., 2019). On a larger scale, the climate in coastal wetlands is influenced by the moderating effects of the adjacent water bodies, which tend to stabilize temperatures and results in elevated humidity levels (Y. Zhang et al., 2019). They often receive substantial precipitation due to the influence of maritime air masses, with clouds and rain storms that can rapidly develop and move through an area.

Traditionally, hydrodynamic processes within coastal wetlands are measured using in-situ water level gauge stations. These gauge networks measure water level changes (WLC) with fast temporal sampling but they are spatially sparse and thus do not provide spatially comprehensive information about hydrodynamics within the wetlands. Remote sensing methods have been applied to improve the spatial coverage. Repeat-pass synthetic aperture radar (SAR) interferometry (InSAR) can enable estimation of WLC in wetlands over large spatial scales because of the presence of emergent vegetation that promotes double-bounce scattering (Lee et al., 2020; Liao et al., 2020; Wdowinski, Hong, & Kim, 2008; Wdowinski, Kim, et al., 2008). InSAR uses interferometry applied to two SAR complex images acquired at different times but from the same viewing angle to determine the change in surface position from the measured change in the phase of the backscattered electromagnetic wave.

The heterogeneity of the Earth's atmosphere induces spatially and temporally random delays to the SAR signal (Hanssen, 1998). Changes in the atmosphere along the imaging path, which include changes in water content, pressure, and temperature, can significantly impact repeat-pass InSAR measurements and may lead to misinterpretation of the phenomena of interest (Bekaert et al., 2015; Danklmayer & Camara de Macedo, 2007; Ferretti

Validation: Saoussen Belhadj-aissa, Talib Oliver-Cabrera
Visualization: Saoussen Belhadj-aissa
Writing – original draft: Saoussen Belhadj-aissa
Writing – review & editing: Saoussen Belhadj-aissa, Marc Simard, Cathleen E. Jones, Talib Oliver-Cabrera, Alexandra Christensen

et al., 2001). These changes can occur in the troposphere or the ionosphere, but water is present mainly in the lower atmosphere. The troposphere is the lowest layer of the Earth atmosphere, which extends from the surface of the Earth up to about 10–15 km. It consists of two distinct components, namely the dry, or hydrostatic, component and the wet component (Bekaert et al., 2015; Murray et al., 2019). The hydrostatic component is dominated by changes in air pressure and temperature and thus correlated with topography. In coastal wetlands, where the terrain is predominantly flat and the climate is moderated by the ocean, variations in pressure and temperature exert less influence, so the related interferometric phase remains relatively uniform across the observation domain and is canceled during interferometry (Hanssen, 2001). However, the wet component is temporally dynamic and spatially complex, with variable water vapor and liquid water content. For example, cumulus clouds have a notable liquid water content ranging from 0.5 to 2.0 g/m^3. This amount of water causes an increase of zenith delays in the range of 0.7–3.0 mm/km (Hanssen, 1998), which is manifested in SAR acquisitions by phase changes that scale linearly with the delay in the signal pathway.

Prior studies characterized the atmosphere and mitigated its effects on InSAR measurements either with or without ancillary data (Bekaert et al., 2015; Berardino et al., 2002; Ferretti et al., 2001; Löfgren et al., 2010; Onn & Zebker, 2006). Some atmospheric InSAR correction methods use ancillary information from weather models (e.g., the archived European Center for Medium-Range Weather Forecasts (ECMWF) ERA-I weather model with an average spacial resolution of 80 km) or spectrometer data (e.g., MERIS and MODIS with a spatial resolution of ≈1.2 and 1 km, respectively) to estimate the tropospheric delay. However, many of these implementations are not suitable for coastal wetland hydrology due to the coarse spatial resolution and the temporal resolution of several hours. Additionally, the sparse spatial coverage of GPS stations relative to the SAR scene size makes it hard to model atmospheric correction using GPS.

None of the atmospheric correction methods adequately account for water content and there is generally a lack of research investigating the wet troposphere's influence on InSAR time series measurements. This phenomenon particularly impacts the accuracy of InSAR studies in coastal regions and other areas where wet troposphere effects dominate. Although a few studies investigated the impact of precipitation on SAR backscatter images (Danklmayer & Chandra, 2009; Koyama et al., 2021; Pierdicca et al., 2013), there has been a notable absence of studies researching the broader influence of precipitation and dense cloud cover on interferometric phase, especially for L-band interferometry.

While persistent scatterer (PS) and Small BAseline Subset (SBAS) time series analyses can reduce atmospheric noise through averaging of random fluctuations (Berardino et al., 2002; Ferretti et al., 2001). However, these methods are insufficient without many PS pixels, with only a few acquisitions, or when the stack contains measurements with short temporal baseline as is used for studying the tidal component of coastal hydrology. These limitations can have an impact on rapid repeat airborne InSAR for which the temporal repeat interval can be very short, even less than 1 hour.

These shortcomings have motivated us to develop an empirical approach to atmospheric noise correction based on Independent Component Analysis (ICA). ICA is a non-orthogonal projection method applicable to multivariate observations. It performs a linear transformation, which consists of the extraction of components while maximizing their independence through a statistical measure of order higher than two (Hyvärinen & Oja, 2000; Jolliffe, 2003). Some studies have used ICA to separate geophysical processes in spaceborne C-band InSAR time series (Cohen-Waeber et al., 2018; Ebmeier, 2016; Gaddes et al., 2018; Maubant et al., 2020; Zhu et al., 2022). However, its potential has not been assessed for airborne L-band InSAR applied to coastal hydrology.

In this paper, we focus on the impact of the atmospheric delay on airborne InSAR, which is affected only by the tropospheric layers below the flight altitude, which can include significant amounts of wet troposphere. We present an ICA-based approach informed by in-situ data to separate the atmospheric and the Water Level Change (WLC) signals within an L-band InSAR time series. The study site includes coastal wetlands in southern Louisiana, an area that experiences a wide range of cloud and precipitation conditions. For example, many coastal areas in Louisiana received between 50 and 60 inches (1,270–1,524 mm) of annual precipitation in 2021 (NOAA National Centers For Environmental Information, States Climate Summaries 2022, https://statesummaries.ncics.org/chapter/la/). The InSAR-derived WLC data set used in this study was derived from L-band SAR data acquired with the Uninhabited Aerial Vehicle SAR (UAVSAR) instrument. The identification of WLC components is achieved through correlation of the eigenvectors of the ICA decomposition with in-situ water level measurements. The WLC-correlated components are used to reconstruct a "filtered" time series, and the remaining

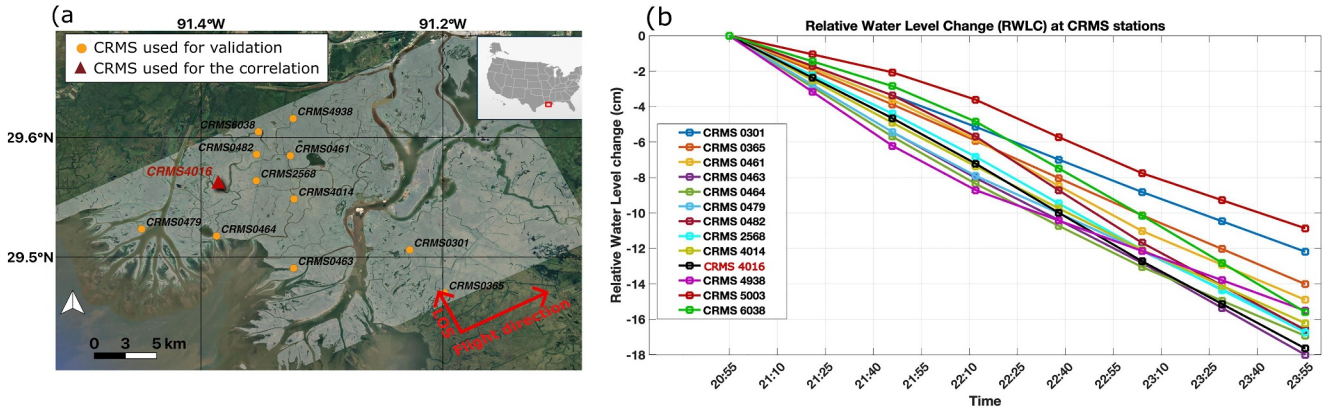

Figure 1. (a) An overview of the study area with the uninhabited aerial vehicle synthetic aperture radar (UAVSAR) scene extent. The delta on the left is the Wax Lake Delta, the terminus of the Wax Lake Outlet. The delta on the right, partially imaged by UAVSAR, is the Atchafalaya River Delta, which is at the end of the Atchafalaya River. The dots show the locations of the coastwide reference monitoring system (CRMS) water gauges. (b) Water level change relative to the value at 20:55 measured at the CRMS gauges. CRMS station 4,016 was chosen for identification of the independent component showing WLC.

components reconstruct a time series of tropospheric delay maps, which are compared to NEXRAD weather radar and tropospheric delay maps generated through the Generic Atmospheric Correction Online Service for InSAR (GACOS). Although the method is developed and demonstrated for a rapid repeat time series of airborne SAR images, it is generally applicable to InSAR-derived displacement time series and can be used to estimate uncorrected atmospheric artifacts for other applications.

2. Data Sets

This study uses data acquired as part of the NASA Earth Venture-Suborbital Delta-X mission to evaluate the potential of ICA to differentiate noise from water level change signals in InSAR. The Delta-X mission studies the processes controlling soil accretion in the Mississippi River Delta (Cortese et al., 2023), an area experiencing rapid relative sea level rise of ≈9 –12 mm/year (Nienhuis et al., 2017). The project calibrates and validates hydrodynamic and morphodynamic models using in-situ and remote sensing measurements from multiples airborne sensors (Jensen et al., 2021; Denbina et al., 2019; X. Zhang et al., 2022; Oliver-Cabrera et al., 2022). UAVSAR acquired SAR images during different parts of the tidal cycle to generate WLC times series using InSAR. The WLC is compared to in-situ water gauge data to identify which ICA components correspond to the true signal and which to noise.

2.1. In-Situ Water Level Data

The measurements used in the ICA process and for the validation come from a network of in-situ water gauges distributed across the study site (Figure 1a).

The Coastwide Reference Monitoring System (CRMS) (Coastal Protection and Restoration Authority (CPRA) of Louisiana, 2023) is a regional-scale ecosystem monitoring system that provides data on wetland hydrology, ecology, soil, and geomorphology for large-scale coastal restoration and management applications in Louisiana (lacoast.gov/crms2/). There are 13 CRMS water level gauge stations within the atchaf_06309 flight footprint. Because all WLC profiles at the CRMS stations in the study area are similar, showing linear trend (Figure 1b), we used one station for correlating WLC with the ICA eigenvectors and used the remaining stations for validation. The selection of the specific station for correlation was arbitrary.

2.2. InSAR-Derived Water Level Change (WLC)

The L3 UAVSAR InSAR Water Level Change Product (Jones et al., 2022) from the NASA Delta-X mission was used for this study. A total of 24 UAVSAR flights of approximately five hour duration each were performed over the Terrebonne and Atchafalaya basins during fall and spring of 2021. The aircraft flew at an altitude of 12.5 km, repeating measurements every 20–40 min during the flight. The data collection campaign captured high-frequency wetland surface dynamics influenced by ocean tides under varying atmospheric conditions. For this study, we use

Table 1
L3 UAVSAR Data Characteristics

Platform	UAVSAR
Flight number	Atchaf_06309
Frequency	L-band $\lambda = 23.8$ cm
Spatial resolution	6 m (along-flight-line) by 6 m (slant range, along line-of-sight (LOS))
Acquisition time	05-Sep-2021 20:55 to 05-Sep-2021 23:58 (8 acquisitions)
Temporal baseline	25–26 min
Site	Atchafalaya Basin, Louisiana, USA

one of the data sets acquired over the Atchafalaya Basin and the northwest corner of Terrebonne Basin during the fall campaign, since the time series for this data set appears to be one of the most affected by the presence of dense clouds and/or precipitation. The data characteristics of the sensor and products are summarized in Table 1.

The method used to generate the WLC products is presented in (Oliver-Cabrera et al., 2022) and described briefly here. After pre-processing the single-look complex (SLC) data to form interferograms using the Interferometric SAR Scientific Computing Environment (ISCE) (https://github.com/isce-framework/isce2) (Rosen et al., 2012), the interferograms are unwrapped and corrected for phase unwrapping errors using the method described in (Oliver-Cabrera et al., 2022). The time series of surface change in the line-of-sight (LOS) direction is generated applying Small BAsline Subset (SBAS) analysis with the Miami INsar Time-series software in PYthon (MintPy) (Yunjun et al., 2019) open-source toolkit (https://github.com/insarlab/MintPy), then the final UAVSAR L3 WLC time series products are generated by projecting the LOS displacements to the vertical direction assuming that all the displacement is from water level change, that is, in the vertical direction (Jones et al., 2022; Oliver-Cabrera et al., 2022). The WLC is relative to the water level at the time of acquisition of the first scene in the time series.

The georeferenced UAVSAR L3 WLC time series acquired on 05-Sep-2021 from 20:55 to 23:55 UTC are shown in Figure 1. Each panel displays the difference in water level relative to the first acquisition for a given time, with negative values (blue color) indicating decreasing water level and positive values (red color) indicating increasing water level. Visually the WLC signal should be recognizable by its shape and location, usually near a water channel or at the land-ocean interface. However, in the time series there are also large-scale features of decreasing and increasing signal that appear unrelated to WLC. Given the shapes and locations of these features, they are likely related to changes in atmospheric delays from the wet troposphere (i.e., rain events or cumulus clouds) (Oliver-Cabrera et al., 2024). The magnitude of the impact on WLC from these changes reaches 15 cm in certain areas of the domain.

2.3. Next Generation Weather Radar (NEXRAD)

To validate the tropospheric delay maps, we used reflectivity maps acquired from the Next Generation Weather Radar (NEXRAD) ground-based weather radar located in New Orleans, Louisiana (Figure 3). The NEXRAD system is a network of 160 high-resolution S-band Doppler weather radars. We downloaded Level-II (L2) reflectivity maps using the freely accessible tool NOAA Weather and Climate Toolkit (www.ncdc.noaa.gov/wct/).

3. Method

In the absence of noise and with only water level change, the interferometric phase difference between two InSAR acquisitions should be proportional to the projection of the WLC, Z, in the LOS direction, as

$$\Delta\varphi = \varphi_1 - \varphi_2 = \varphi_{\mathrm{WLC}} = \frac{4\pi}{\lambda}(R_1 - R_2) = \frac{4\pi}{\lambda} Z \cdot \cos\theta, \quad (1)$$

where R_1 and R_2 correspond to the one-way sensor-target distance on the first and second acquisitions, λ is the radar wavelength, and θ is the incidence angle (Figure 4).

10.1029/2024EA003540

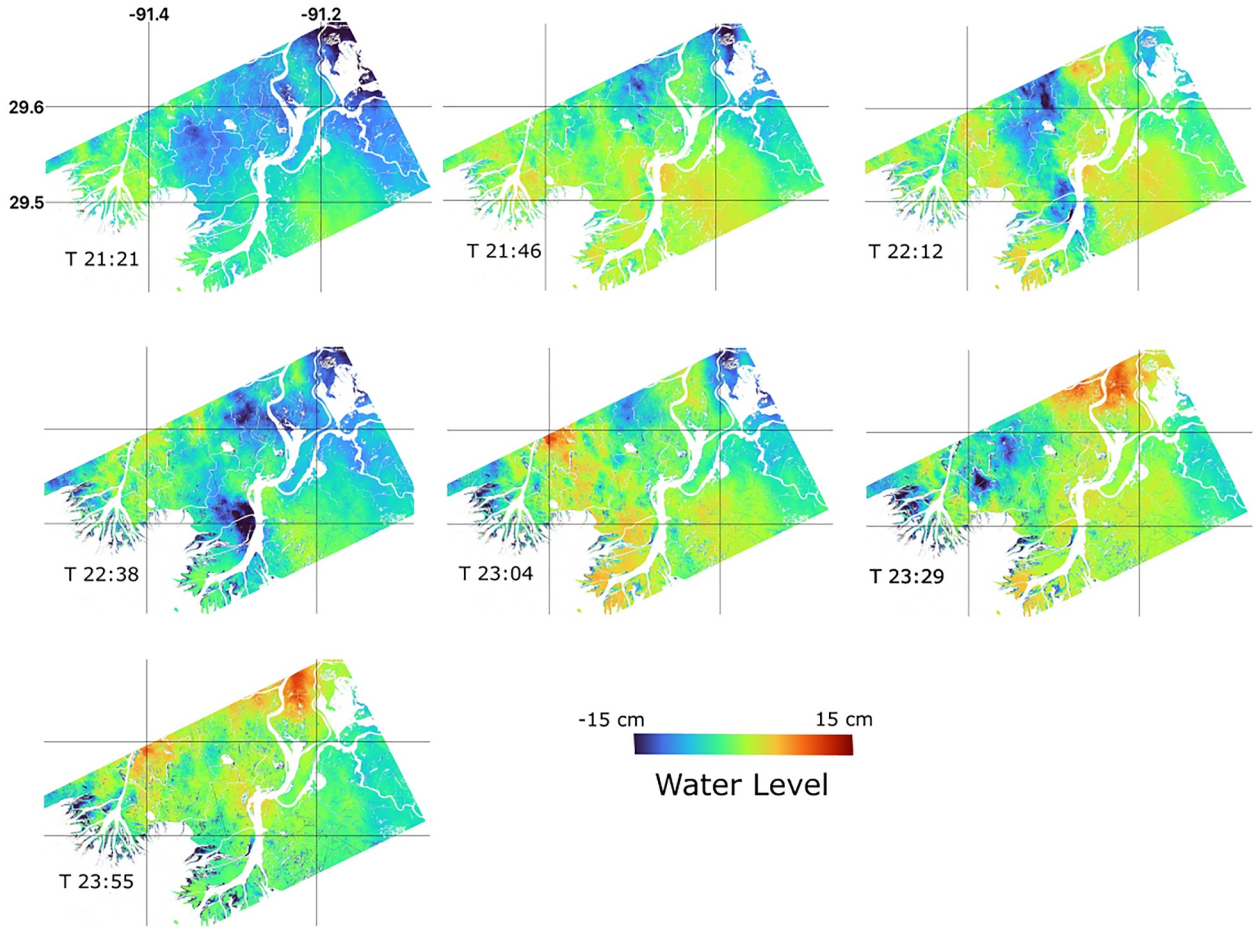

Figure 2. Delta-X uninhabited aerial vehicle synthetic aperture radar L3 water level change time series (Jones et al., 2022) showing change relative to the first acquisition at 20:55.

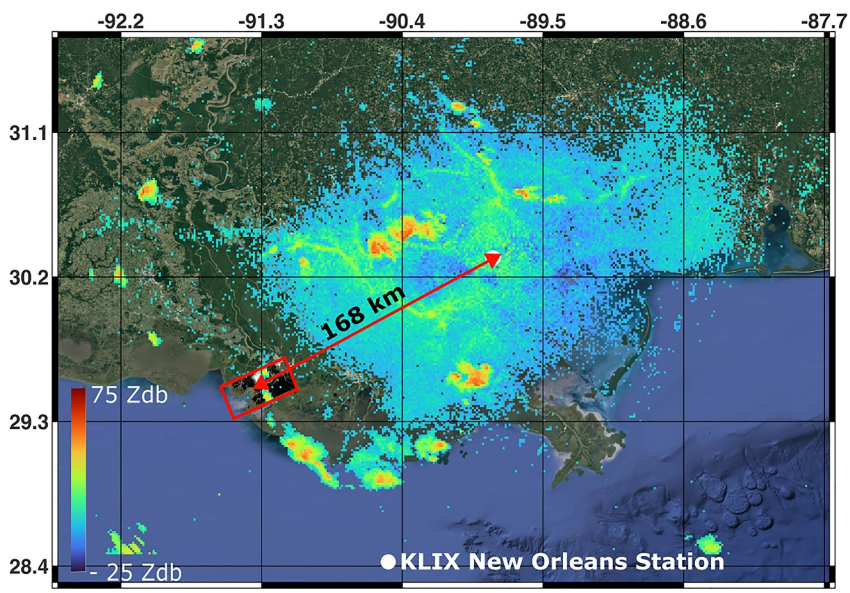

Figure 3. Reflectivity map at time 22:10 from the New Orleans NEXRAD station showing the distance between the station and the uninhabited aerial vehicle synthetic aperture radar footprint.

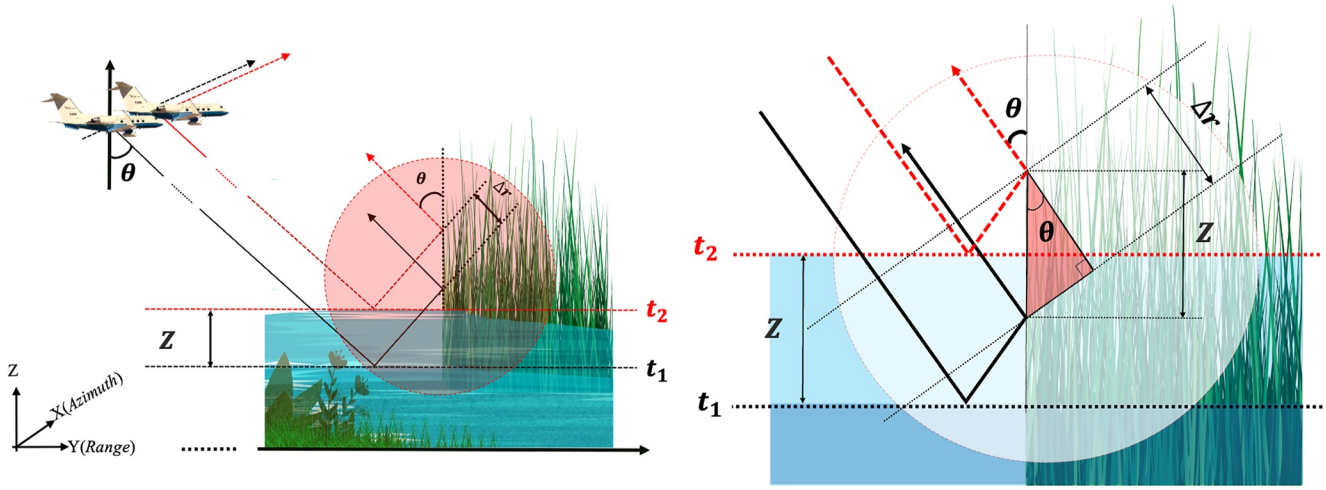

Figure 4. InSAR geometry to measure water level change in wetlands.

However, the spatial and temporal atmospheric heterogeneity in the troposphere causes changes in the index of refraction of the atmosphere, changing the effective path length through the atmosphere. For simplicity, hereafter, the tropospheric effects will be referred as "atmospheric effects." Accounting for this, the measured interferometric phase, φ_{in}, becomes

$$\varphi_{\text{in}} = \frac{4\pi}{\lambda} Z \cdot \cos\theta + \frac{4\pi}{\lambda}(\Delta_{atm}), \tag{2}$$

where Δ_{atm} is the relative difference in atmospheric delays of radar signals corresponding to the first and second acquisitions. This variation is manifested by a bias ranging from a few millimeters to several centimeters (Hanssen, 1998). There are other potential sources of bias in the signal that enter into the term Δ_{atm}, for example, phase unwrapping errors, topography, or aircraft position. These sources are not included explicitly for three reasons: (a) the topography varies little over the wetland study site; (b) the phase unwrapping errors are corrected using a method specifically designed for measuring water level change in wetlands (Oliver-Cabrera et al., 2022); and (c) aircraft position errors are estimated and removed during UAVSAR data processing (Jones et al., 2009). For these reasons, the main InSAR error source in the rapid repeat time series should be atmosphere. Additional sources relevant to spaceborne instruments are ionospheric delay and orbital errors which are not considered here.

The application of ICA to a WLC time-series consists of estimating the following generative model of the data: Considering the N elements of the water level change time series ($N = 7$ in our case) acquired at times t_n, each measured value without correction, Z_m, for a resolution cell located at (x, y) can be written as

$$Z_m(x,y,t_n) = \hat{Z} + \hat{\Delta}_{atm}, \tag{3}$$

where $\hat{Z}$ represents the estimated filtered WLC using ICA, presumably close to the real WLC, and $\hat{\Delta}_{atm}$ is the residual, assumed to be the relative atmospheric delay.

After vectorizing the WLC maps to N input vectors X of length P, where P is the number of pixels in each map, the ICA assumes that each of the N vectors can be formulated as a mixture of at most N independent vectors S (score vectors) as:

$$[X] = [A] \times [S], \tag{4}$$

where $X \in R^{N,P}$ (real matrix of dimension N × P) and $A \in R^{N.M}$ is the mixing matrix. To find S, the equation is inverted as

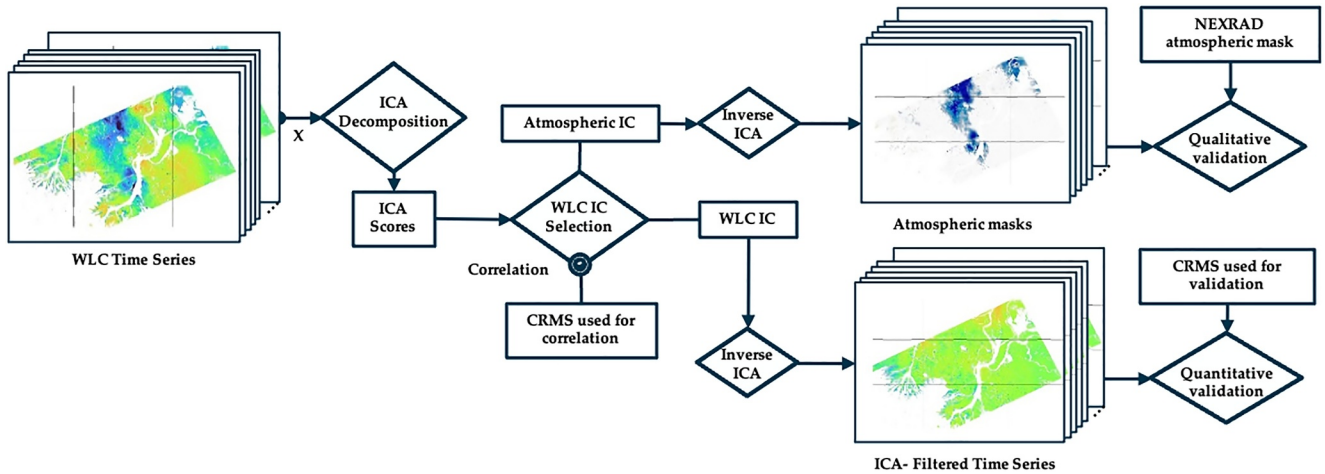

Figure 5. Flowchart showing the application of independent component analysis guided by in-situ measurements for differentiating true water level change (WLC) from atmospheric artifacts when using InSAR.

$$[S] = [W] \times [X] \tag{5}$$

where $W \in R^{N,M}$ is the inverse of A, and M is the number of Independent Components (IC) of $S \in R^{M,P}$ to generate. In this case $M = N$ because we are generating the same number of IC S as input images X.

The statistical independence of the components is characterized by a measure of non-Gaussianity that is formulated by using a contrast function. Our initial selection for the contrast function was the kurtosis. However, due to the small number of images in the time series and the susceptibility of the kurtosis to outliers, we opted to use the negentropy with the hyperbolic tangent (*Tanh*) function. This choice was motivated by the ability of the *Tanh* function to distinguish between various types of non-Gaussian distributions, from sub-Gaussian to super-Gaussian distributions (Hyvarinen, 1999). The application of ICA decomposition on the WLC time series presented in Figure 2 was achieved using a fastICA algorithm (Hyvarinen, 1999) with the hyperbolic tangent as a contrast function.

Under the assumption that the spatio-temporal distributions of WLC and atmospheric delay should be distinguishable and independent from each other, applying the ICA as a blind source separation allows their effective dissociation. However, ICA does not determine the order of the generated components through their variances, since the variances of all generated IC are unitary. Therefore, the components obtained need further interpretation to determine the signal they represent. For this, we propose a decision-making step to automatically determine which component(s) represent the water level change signal by the integration of in-situ measurements.

Selecting the components that represent WLC signal using in-situ measurements is achieved through the computation of the coefficient of correlation, R^2, between in-situ relative WLC and the eigenvectors of the mixing matrix, W. After identifying the IC corresponding to WLC, the filtered time series of WLC is generated through ICA inversion using only the WLC components. The remaining components are then used to generate a time series of tropospheric delay maps.

The application of ICA as an atmospheric signal filtering technique is summarized in the flowchart shown in Figure 5. We validate the approach by comparing the INSAR-estimate of WLC before and after the ICA-based filtering with the in-situ measurements. We use residual errors and the signal-to-noise ratio before and after the filtering as performance metrics.

4. Results and Discussion

Figure 6 shows the resulting IC score images, which are the vectors S once rasterized, and the eigenvectors of the mixing matrix W. Each IC score image shows a different spatial distribution representing independent sources, and the eigenvector of the IC represents its temporal trend. The temporal variation of the water level should be

10.1029/2024EA003540

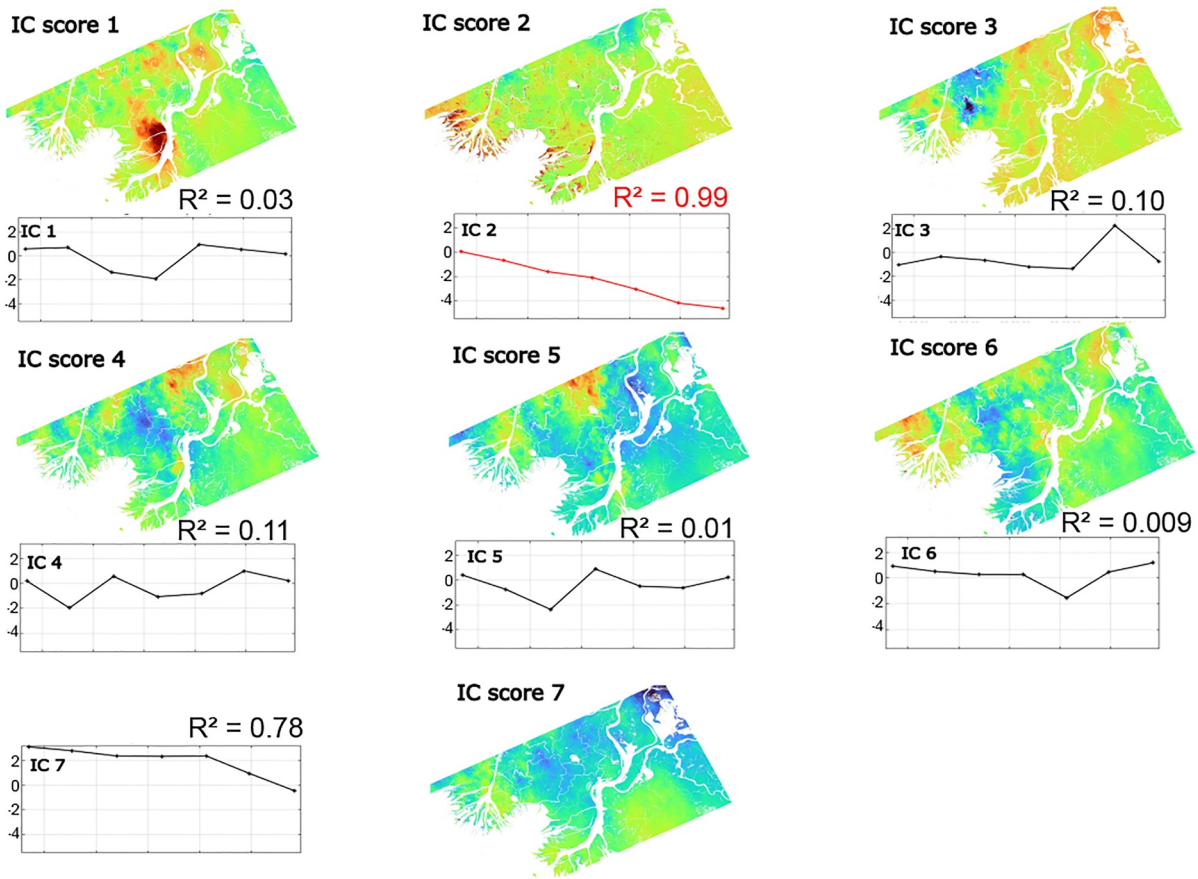

Figure 6. Independent Component score images and eigenvectors. The chosen IC's eigenvector is plotted in red.

recognizable in at least one of the eigenvectors (Figure 6) if the ICA decomposition effectively separated all spatial distributions present in the time series.

At this stage of the process, we calculate the cross correlation between each eigenvector and the CRMS WLC in order to identify ICs strongly associated with WLC. From the R^2 correlation results shown in Figure 6, the second component (IC2) with a correlation of 99% is selected. At this step, the threshold was set to 80% and was determined experimentally on the basis of the maximum correlation between the IC eigenvectors and the In-situ Water Level Change signal after implementing the proposed workflow on the WLC time series shown in Figure 2 and from other Delta-X flight dates (see Supplement). We note that the choice of a relatively high threshold was also driven by the fact that there are only eight images in the time series, so the IC eigenvectors have few points. A lower threshold could be used with more images.

After selecting the IC eigenvector(s) representing WLC signals, an inverse ICA is performed to reconstructa time series of "filtered" WLC. Figure 7 shows the filtered WLC time series reconstructed with the selected IC component, IC2. This series no longer has some of the large features that are present in the initial time series (Figure 1), and shows decreasing water levels in the wetlands near where the Wax Lake Outlet and the Atchafalaya River flow into the Gulf of Mexico, in the southern part of the study domain. However, there remains an increasing signal in the northeast that is present in all time series, which reaches 10 cm in the last map. This is likely related to an atmospheric delay present in the reference image used to form all the interferograms. This occurs when the atmospheric delay present in the reference image remains throughout the time series, the linear component of the atmospheric delay was separated in the same component as the WLC signal, which is also changing linearly in time.

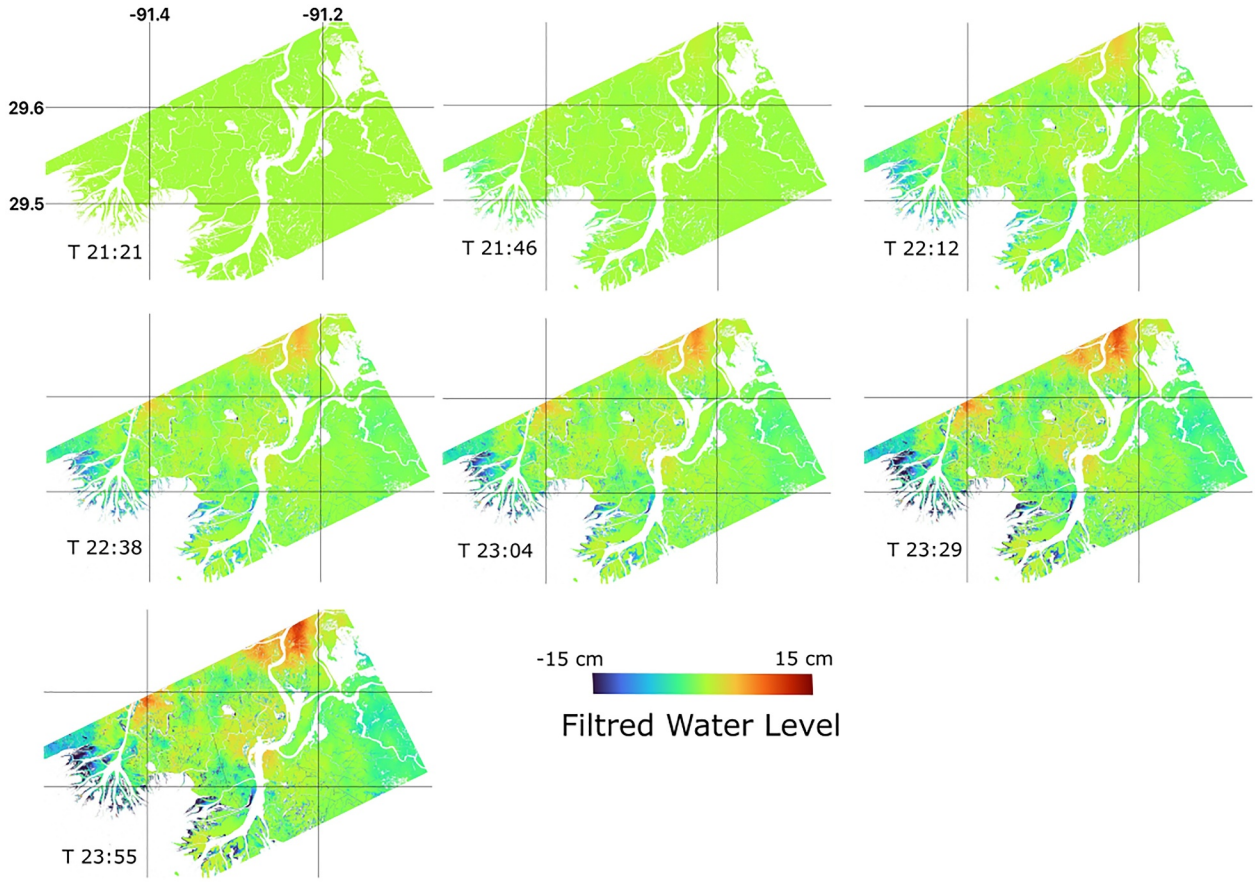

Figure 7. Independent component analysis filtered WLC time series.

As described in the flowchart in Figure 5, the remaining ICs were associated with atmospheric delay according to Equation 3 and used to reconstruct a time series of likely atmospheric artifacts (Figure 8).

4.1. Validation

4.1.1. Water Level Change

To validate our approach, we used the 12 remaining CRMS stations' in-situ water level measurements as ground truth. The temporal profiles of WLC from in-situ measurements (blue), original unfiltered WLC (red), and filtered WLC (black) are plotted in Figure 9 for each of the 12 stations. Most of the profiles before the filtering are much noisier than the in-situ profiles. In contrast, the ICA filtered WLC profiles are less noisy and exhibit a stronger correlation with the trend of the in-situ measurements. These qualitative observations are quantitatively evaluated with metrics Root Mean Square Error (RMSE), Mean Absolute Error (MAE), Coefficient of Determination (R^2), and Signal-to-Noise Ratio (SNR) before and after ICA filtering, reported in Figure 10. These metrics are calculated with respect to the in-situ measurements.

The RMSE and MAE bar plots provide a quantitative measure of the errors and discrepancies between the in-situ measurements, the original WLC, and the filtered WLC. The RMSE is reduced for all sites, by approximately 2–4 cm for CRMS0365, CRMS0461, CRMS0464, CRMS2568 and CRMS4938, and by 5–7 cm for the remaining stations. The MAE, which quantifies absolute errors instead of quadratic errors, is similarly reduced. The correlation coefficient, R^2, for all stations is better correlated with the in-situ WLC after filtering, with a value of 99%. The SNR is a typical metric used to evaluate a filtering method. In our test case, the most significant improvement is for CRMS6038 (RMSE of 5 cm), for which the SNR is improved from 2.6 to 16 dB. At other stations, the SNR of the filtered WLC ranges from 4 to 15 dB, compared to an SNR ranging from −3 to 9 dB before filtering. However, for station CRMS0479 and CRMS0463 highlighted in red in Figure 10, there is improvement of the R^2

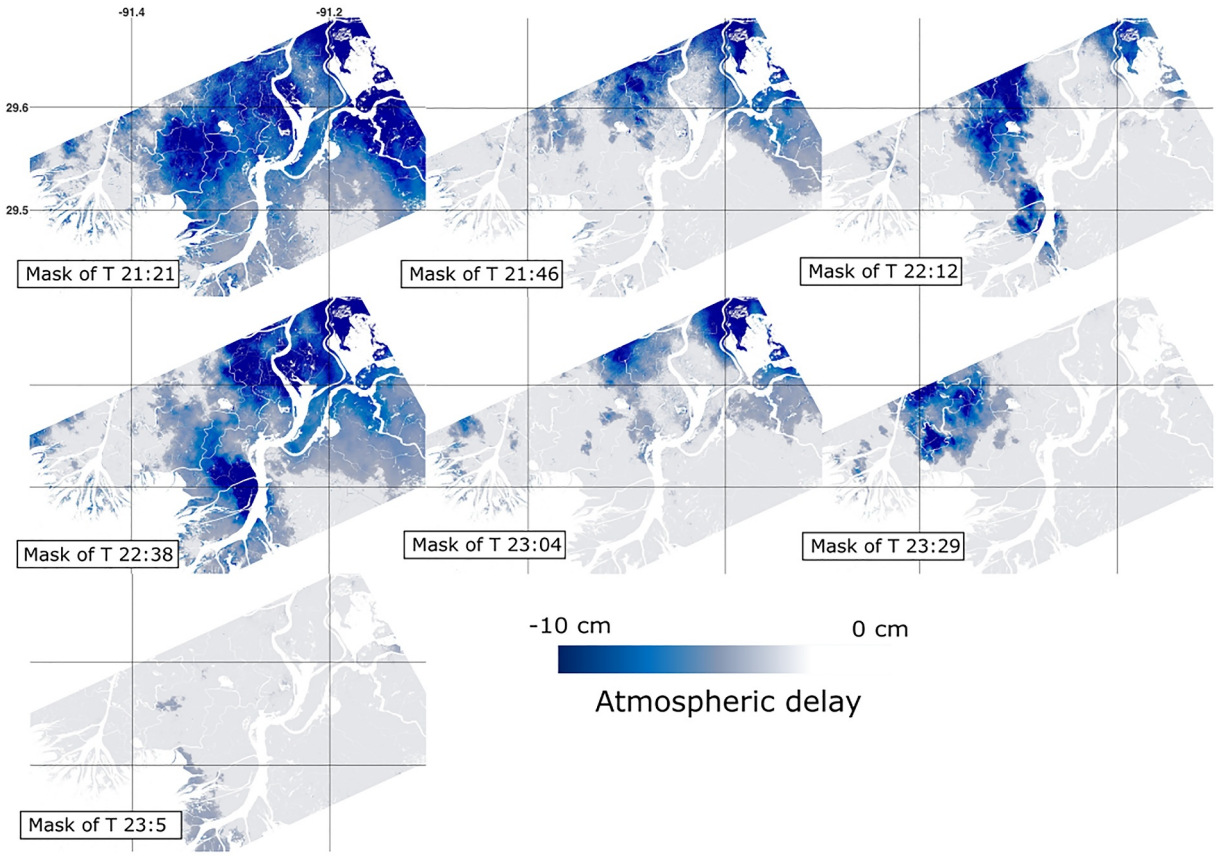

Figure 8. Tropospheric delay maps generated through the proposed approach.

after the filtering, but the SNR, RMSE, and MAE metrics are not improved. Although the original WLC at CRMS0463 is noisy, the fact that the average is closer to the in-situ compared to the filtered WLC results in lower RMSE before the filtering. At CRMS0479 the original WLC is the least noisy due to the fact that this area contains almost no atmospheric artifacts.

4.1.2. Atmospheric Delay

Reflectivity measurements from the NEXRAD weather radar $\lambda = 10.7$ cm) located in New Orleans, Louisiana, are used for validation of the generated tropospheric delay maps. The NEXRAD reflectivity values are divided into categories to describe different intensities of precipitation. Negative values, such as -10 dBZ, indicate very weak radar echoes, typically associated with light drizzle or very light rain. As the reflectivity values increase, the precipitation intensity also increases (Binetti et al., 2022).

Although we compare the SAR tropospheric delay maps generated through ICA with NEXRAD reflectivity, we note that there is a substantial difference in the imaging geometries of the two sensors. The airborne SAR is imaging the ground through the clouds with a side-looking geometry so the clouds do not project directly on the ground below, but are offset by an amount that depends upon their height, the height of the aircraft, and the instrument look angle. The NEXRAD is ground-based and images only the atmosphere from a much greater distance, with varying height range depending upon the distance from the radar. In fact, the ground-based radar acquires reflectivity at different altitudes, but the minimum altitude increases with increasing range from the radar. Furthermore, the NEXRAD minimum detectable reflectivity decreases as the range increases. Therefore, exact spatial overlap between features is not expected (Oliver-Cabrera et al., 2024).

Figure 11 shows two of the ICA-based tropospheric delay maps compared to two NEXRAD reflectivity maps acquired at the same time, showing qualitative correlation between spatial features present in both maps. Nevertheless, some feature observed in the northeast part of the domain in the ICA-based maps are not observed

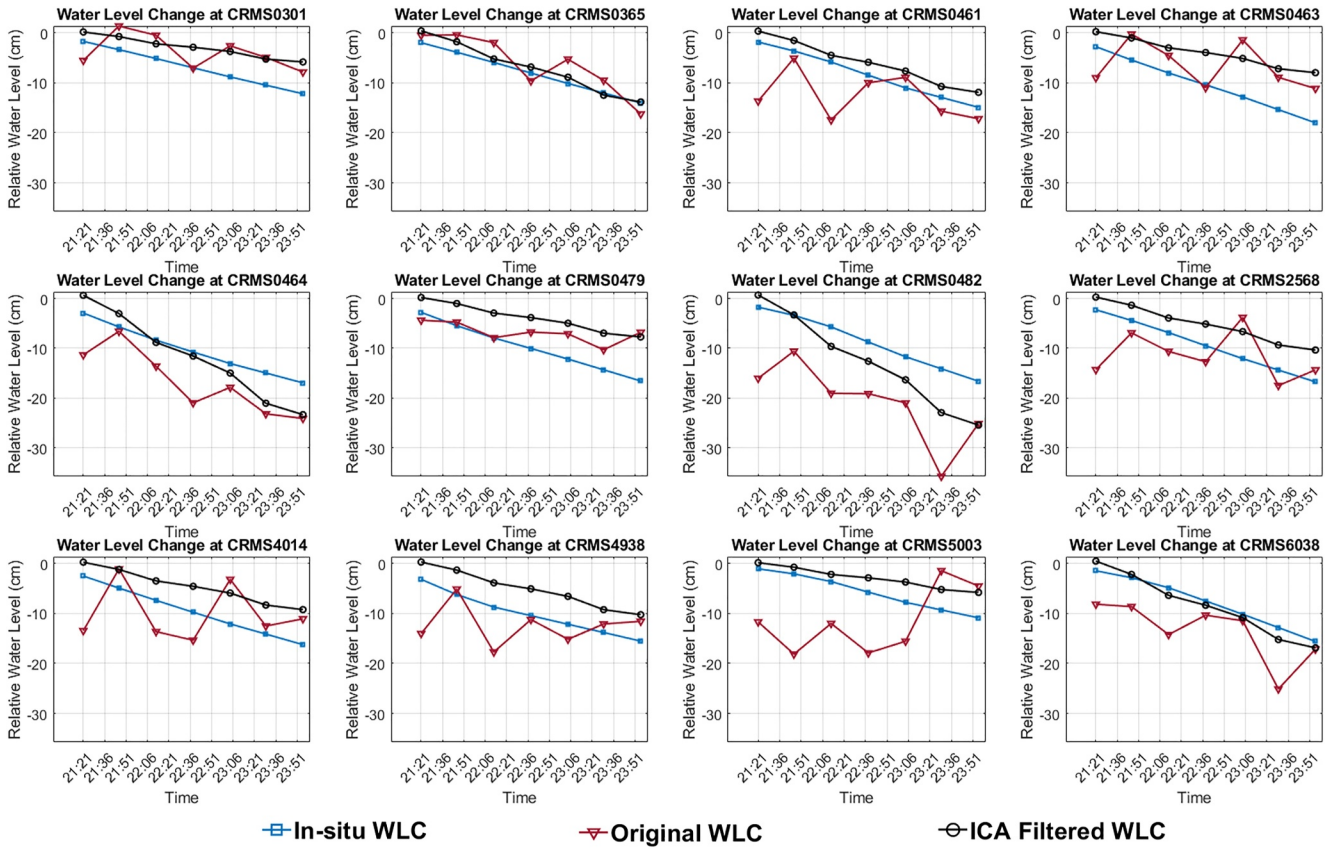

Figure 9. In-Situ WLC compared to original and ICA-filtered WLC.

in the NEXRAD reflectivity maps. The difference in viewing geometry and target-sensor distances between UAVSAR and NEXRAD precludes precise correlation of all of the obtained atmospheric delay maps with the NEXRAD weather maps, however the general correspondence of the features is apparent. The ICA-based maps identify wet troposphere signal in the northeast that is not seen by NEXRAD, particularly at time 22:36. It is not known if this is because the NEXRAD radar did not detect clouds or if this is another source of noise.

Figure 11 also compares the masks to a standard InSAR atmospheric correction product, the GACOS tropospheric delay map derived using the High Resolution European Center for Mid-Range Weather Forecasts (ECMWF) weather model at 0.1° spatial resolution and 6-hr temporal resolution (Yu et al., 2017; Yu, Li, & Penna, 2018; Yu, Li, Penna, & Crippa, 2018). Corrections based on this product would not reduce the atmospheric noise signal in regions where clouds are detected by NEXRAD.

We can estimate the integrated water vapor content (IWV) at the location of the maximum atmospheric delay based on the relationship

$$\mathrm{IWV} = \frac{\lambda}{4\pi} \cdot \phi_{\mathrm{atm}} \cdot \cos(\theta_{\mathrm{inc}}) \cdot \Pi \tag{6}$$

where IWV is in mm and Π is a function of the mean atmospheric temperature (Alshawaf et al., 2015; Bevis et al., 1994). Given the estimated atmospheric delay of −10 cm, incident angle at the specified location of $\theta = 40°$, and considering that the atmosphere temperature at the cloud's altitude is ≈277–283 K based upon a surface air temperature of ≈306.76 K, we estimate IWV ranging from 9.2 to 9.5 mm. This estimate closely aligns with the maximum precipitation recorded on the date of the UAVSAR time series for this location, based on data obtained from the NOAA Weather and Climate Toolkit.

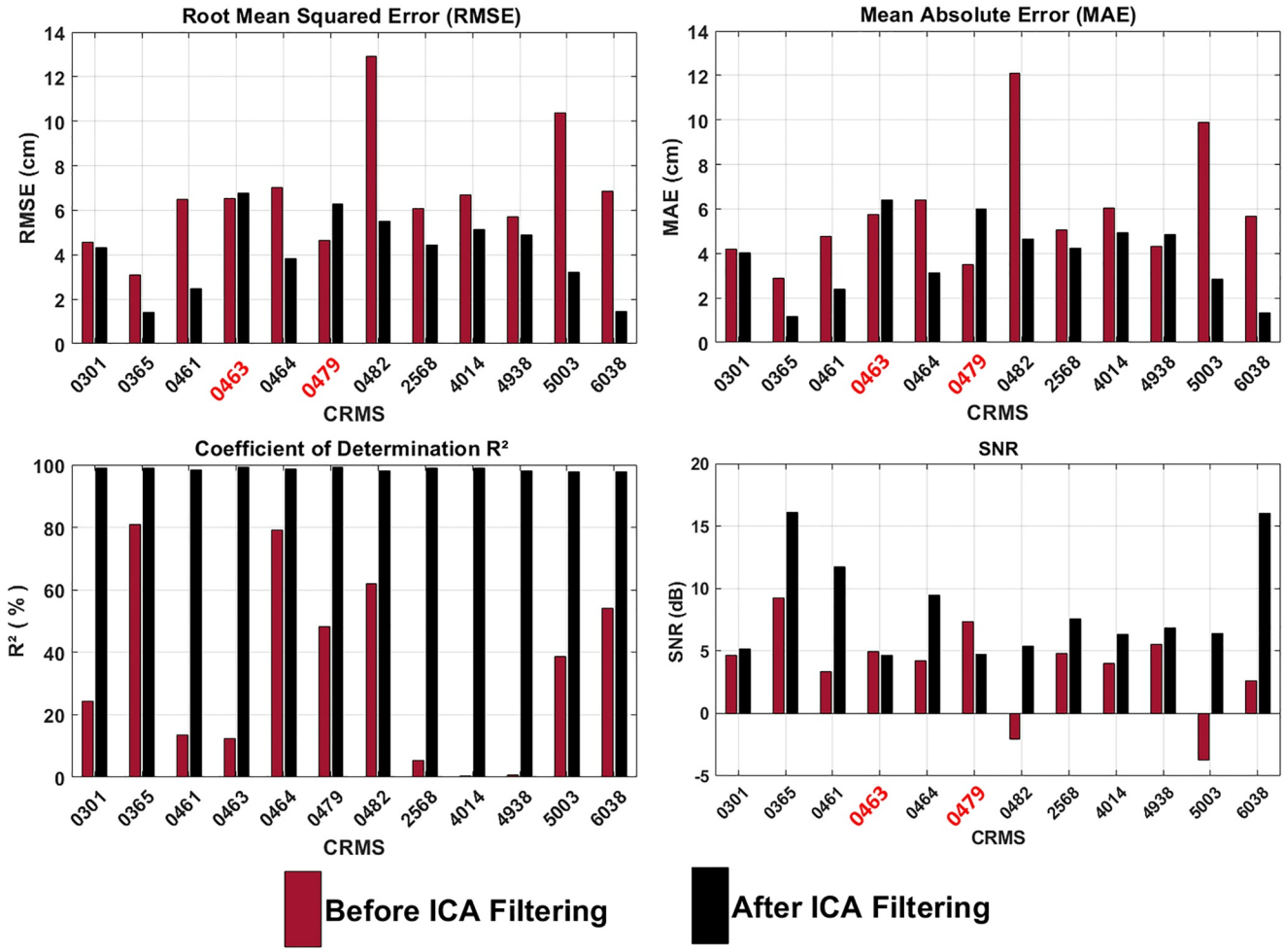

Figure 10. Comparison of root mean square error, mean absolute error, R^2, and SNR before and after independent component analysis filtering for each coastwide reference monitoring system station. Stations labeled in red in specific plots show instances where the values did not improve after filtering.

5. Conclusions

This work presents an alternative solution to the conventional atmospheric correction methods that can remove wet tropospheric noise in InSAR surface displacement time series. InSAR is a valuable tool for measuring WLC within coastal wetlands and can be used to study the hydrodynamics in these complex areas. However, the wet component of the troposphere introduces significant biases in the InSAR measurements that impact the accuracy of the derived WLC. Accuracy of a few centimeters is needed for Delta-X hydrodynamic model calibration. Within the scope of NASA's Delta-X project, UAVSAR acquisitions were used to generate time series of water level change over coastal wetlands in Louisiana to support hydrodynamic model development. Nevertheless, some of the Delta-X InSAR-derived WLC time series showed artifacts, likely due to atmospheric delays, of as much as −15 cm and in some cases exceeding the scale of real WLC expected for the area. Using conventional methods exploiting weather models or GPS to correct these delays is not effective given their coarse spatial and temporal resolution or the unavailability of the data.

In this work, we used an empirical approach that allows blind source separation based on ICA. Using ICA, we were able to separate the signals within the original UAVSAR WLC time series into a filtered WLC time series and likely atmospheric delays. To automatically identify the signals representing WLC, in-situ measurements from water level gauges were correlated with the eigenvectors of the ICA to determine the ICs representing real WLC. This process allowed us to generate a filtered time series of WLC and a time series of atmospheric features from the uncorrelated components.

10.1029/2024EA003540

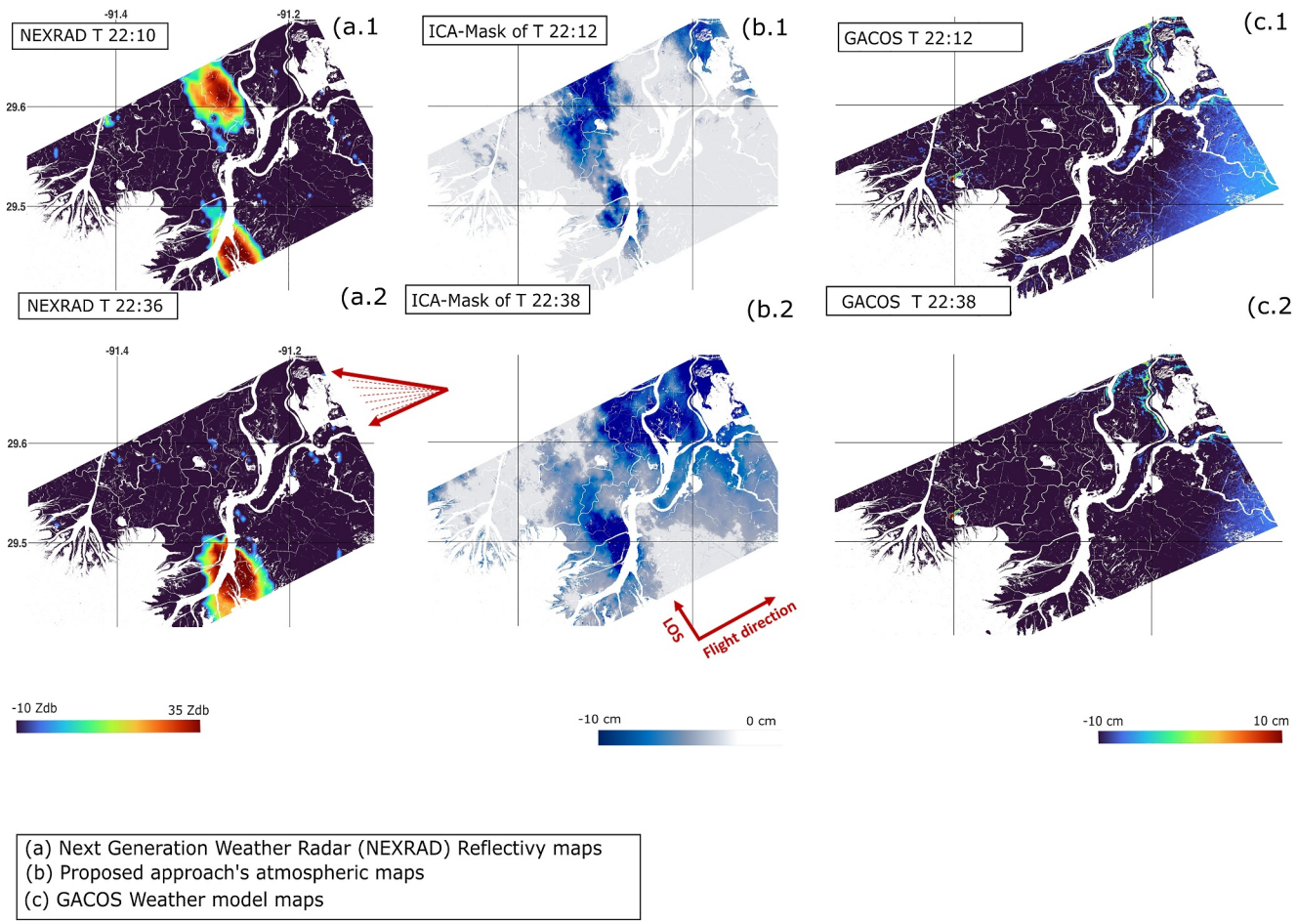

Figure 11. Reflectivity maps from the NEXRAD ground-based weather radar (left) compared to the ICA-derived tropospheric delay maps (center) and tropospheric delay maps generated from the GACOS weather model (right). Red arrows indicate the look direction of the NEXRAD and uninhabited aerial vehicle synthetic aperture radar (see text). The comparison is shown for two times separated by 26 min. The weather model is unable to capture change on this timescale.

The results of the method were validated using in-situ measurements and reflectivity maps from ground-based NEXRAD weather radar. The comparative analysis showed qualitative and quantitative improvement of WLC measurements with a reduction of the average RMSE from 10 to 4 cm. Additionally, improved SNR and R^2 support the effectiveness of the approach. Comparison of reflectivity maps from weather radar to the ICA-based tropospheric delay maps showed reasonable agreement between large-scale and large-value apparent artifacts in the original WLC time series despite differences between the two sensors acquisition modes, sensor parameters, and imaging geometries.

This study assessed the performance of the ICA and in-situ measurements to automatically identify and correct wet troposphere noise and delay in InSAR-derived products. While we demonstrated the performance of the ICA-based atmospheric detection and correction approach for retrieval of WLC, it could be used to improve land surface displacement measurements using GNSS to identify the IC representing true ground movement. Our method is directly relevant to upcoming L-band spaceborne missions, such as NISAR, to improve InSAR ground displacement products and could also be used to study the atmosphere as the signal of interest.

Data Availability Statement

All data used for this study are available for public use.

- The UAVSAR L3 Water Level Change products are available on the ORNL DACC at https://doi.org/10.3334/ORNLDAAC/2058 (Jones et al., 2022).
- The CRMS data on water level Change in Louisiana can be found at, http://lacoast.gov/crms2/home.aspx.
- The NEXRAD Reflectivity map were generated using NOAA Weather and Climate toolkit which can be found at, https://www.ncdc.noaa.gov/wct/.

Acknowledgments
This work was carried out at the Jet Propulsion Laboratory, California Institute of Technology under contract with the U.S. National Aeronautics and Space Administration (NASA). © 2024. Government sponsorship acknowledged. The NASA Delta-X project is funded by the Science Mission Directorate's Earth Science Division through the Earth Venture Suborbital-3 Program NNH17ZDA001N-EVS3.

References

Alshawaf, F., Fersch, B., Hinz, S., Kunstmann, H., Mayer, M., & Meyer, F. (2015). Water vapor mapping by fusing InSAR and GNSS remote sensing data and atmospheric simulations. *Hydrology and Earth System Sciences*, *19*(12), 4747–4764. https://doi.org/10.5194/hess-19-4747-2015

Bekaert, D., Walters, R., Wright, T., Hooper, A., & Parker, D. (2015). Statistical comparison of InSAR tropospheric correction techniques. *Remote Sensing of Environment*, *170*, 40–47. https://doi.org/10.1016/j.rse.2015.08.035

Berardino, P., Fornaro, G., Lanari, R., & Sansosti, E. (2002). A new algorithm for surface deformation monitoring based on small baseline differential SAR interferograms. *IEEE Transactions on Geoscience and Remote Sensing*, *40*(11), 2375–2383. https://doi.org/10.1109/tgrs.2002.803792

Bevis, M., Businger, S., Chiswell, S., Herring, T., Anthes, R., Rocken, C., & Ware, R. (1994). GPS meteorology: Mapping zenith wet delays onto precipitable water. *Journal of Applied Meteorology*, *33*(3), 379–386. https://doi.org/10.1175/1520-0450(1994)033⟨0379:GMMZWD⟩2.0.CO;2

Binetti, M. S., Campanale, C., Massarelli, C., & Uricchio, V. F. (2022). The use of weather radar data: Possibilities, challenges and advanced applications. *Earth*, *3*(1), 157–171. https://doi.org/10.3390/earth3010012

Coastal Protection and Restoration Authority (CPRA) of Louisiana. (2023). Coastwide reference monitoring system (CRMS). *Coastal Information Management System (CIMS) database*. Retrieved from https://cims.coastal.louisiana.gov

Cohen-Waeber, J., Burgmann, R., Chaussard, E., Giannico, C., & Ferretti, A. (2018). Spatiotemporal patterns of precipitation-modulated landslide deformation from independent component analysis of InSAR time series. *Geophysical Research Letters*, *45*(4), 1878–1887. https://doi.org/10.1002/2017GL075950

Cortese, L., Donatelli, C., Zhang, X., Nghiem, J. A., Simard, M., Jones, C. E., et al. (2023). Coupling numerical models of deltaic wetlands with AirSWOT, UAVSAR, and AVIRIS-NG remote sensing data. *Biogeosciences Discussions*, *2023*, 1–28.

Danklmayer, A., & Camara de Macedo, K. (2007). An investigation on atmospheric effects in airborne interferometric SAR data. In *Proceedings of FRINGE*.

Danklmayer, A., & Chandra, M. (2009). Precipitation induced signatures in SAR images. In *2009 3rd European Conference on Antennas and Propagation* (pp. 3433–3437). IEEE.

Denbina, M., Simard, M., Rodriguez, E., Wu, X., Chen, A., & Pavelsky, T. (2019). Mapping water surface elevation and slope in the Mississippi River Delta using the AirSWOT Ka-band interferometric synthetic aperture radar. *Remote Sensing*, *11*(23), 2739. https://doi.org/10.3390/rs11232739

Ebmeier, S. (2016). Application of independent component analysis to multitemporal InSAR data with volcanic case studies. *Journal of Geophysical Research: Solid Earth*, *121*(12), 8970–8986. https://doi.org/10.1002/2016jb013765

Ferretti, A., Prati, C., & Rocca, F. (2001). Permanent scatterers in SAR interferometry. *IEEE Transactions on Geoscience and Remote Sensing*, *39*(1), 8–20. https://doi.org/10.1109/36.898661

Gaddes, M. E., Hooper, A., Bagnardi, M., Inman, H., & Albino, F. (2018). Blind signal separation methods for InSAR: The potential to automatically detect and monitor signals of volcanic deformation. *Journal of Geophysical Research: Solid Earth*, *123*(11), 10226–10251. https://doi.org/10.1029/2018JB016210

Giosan, L., Syvitski, J., Constantinescu, S., & Day, J. (2014). Climate change: Protect the world's deltas. *Nature*, *516*(7529), 31–33. https://doi.org/10.1038/516031a

Hanssen, R. (1998). *Atmospheric heterogeneities in ERS tandem SAR interferometry*. DEOS Report No.98.1 (Tech. Rep.). Delft University press.

Hanssen, R. (2001). Remote sensing and digital image processing. Radar interferometry: Data interpretation and error analysis. *Earth and Environmental Science*, *2*, 200–210.

Hopkinson, C. S., Wolanski, E., Cahoon, D. R., Perillo, G. M., & Brinson, M. M. (2019). Chapter 1 - coastal wetlands: A synthesis. In G. M. E. Perillo, E. Wolanski, D. R. Cahoon, & C. S. Hopkinson (Eds.), *Coastal wetlands* (2nd ed., pp. 1–75). Elsevier. https://doi.org/10.1016/B978-0-444-63893-9.00001-0

Hyvarinen, A. (1999). Fast and robust fixed-point algorithms for independent component analysis. *IEEE Transactions on Neural Networks*, *10*(3), 626–634. https://doi.org/10.1109/72.761722

Hyvärinen, A., & Oja, E. (2000). Independent component analysis: Algorithms and applications. *Neural Networks*, *13*(4–5), 411–430. https://doi.org/10.1016/s0893-6080(00)00026-5

Jankowski, K., Törnqvist, T., & Fernandes, A. (2017). Vulnerability of Louisiana's coastal wetlands to present-day rates of relative sea-level rise. *Nature Communications*, *8*(1), 14792. https://doi.org/10.1038/ncomms14792

Jensen, D., Cavanaugh, K. C., Simard, M., Christensen, A., Rovai, A., & Twilley, R. (2021). Aboveground biomass distributions and vegetation composition changes in Louisiana's Wax Lake Delta. *Estuarine, Coastal and Shelf Science*, *250*, 107139. https://doi.org/10.1016/j.ecss.2020.107139

Jolliffe, I. T. (2003). Principal component analysis. *Technometrics*, *45*(3), 276.

Jones, C., Hensley, S., & Michel, T. (2009). Topography-dependent motion compensation: Application to UAVSAR data. In *2009 IEEE Radar Conference* (pp. 1–6). IEEE. https://doi.org/10.1109/RADAR.2009.4977084

Jones, C., Oliver-Cabrera, T., Simard, M., & Lou, Y. (2022). *Delta-X: UAVSAR L3 water level changes, MRD, Louisiana, 2021*. ORNL Distributed Active Archive Center. https://doi.org/10.3334/ORNLDAAC/2058

Koyama, C. N., Watanabe, M., Tadono, T., & Shimada, M. (2021). Assessing the impact of precipitation on L-band SAR forest observation: An ALOS-2 big data case study in the tropics. In *EUSAR 2021; 13th European Conference on Synthetic Aperture radar* (pp. 1–6). VDE.

Lee, H., Yuan, T., Yu, H., & Jung, H. C. (2020). Interferometric SAR for wetland hydrology: An overview of methods, challenges, and trends. *IEEE Geoscience and Remote Sensing Magazine*, *8*(1), 120–135. https://doi.org/10.1109/MGRS.2019.2958653

Liao, T.-H., Simard, M., Denbina, M., & Lamb, M. P. (2020). Monitoring water level change and seasonal vegetation change in the coastal wetlands of Louisiana using L-band time-series. *Remote Sensing*, *12*(15), 2351. https://doi.org/10.3390/rs12152351

Löfgren, J. S., Björndahl, F., Moore, A. W., Webb, F. H., Fielding, E. J., & Fishbein, E. F. (2010). Tropospheric correction for InSAR using interpolated ECMWF data and GPS zenith total delay from the Southern California integrated GPS network. In *2010 IEEE International geoscience and remote sensing symposium* (pp. 4503–4506). IEEE.

Maubant, L., Pathier, E., Daout, S., Radiguet, M., Doin, M.-P., Kazachkina, E., et al. (2020). Independent component analysis and parametric approach for source separation in InSAR time series at regional scale: Application to the 2017–2018 slow slip event in Guerrero (Mexico). *Journal of Geophysical Research: Solid Earth*, *125*(3). https://doi.org/10.1029/2019JB018187

Murray, K. D., Bekaert, D. P., & Lohman, R. B. (2019). Tropospheric corrections for InSAR: Statistical assessments and applications to the Central United States and Mexico. *Remote Sensing of Environment*, *232*, 111326. https://doi.org/10.1016/j.rse.2019.111326

Nienhuis, J. H., Törnqvist, T. E., Jankowski, K. L., Fernandes, A. M., & Keogh, M. E. (2017). A new subsidence map for coastal Louisiana. *Geological Society of America Today*, *27*(9), 58–59.

Oliver-Cabrera, T., Jones, C. E., Simard, M., Varugu, B., & Belhadj-aissa, S. (2024). Identification of wet troposphere delay in L-band InSAR measurements. *Journal of Geodesy*. (Under Review).

Oliver-Cabrera, T., Jones, C. E., Yunjun, Z., & Simard, M. (2022). InSAR phase unwrapping error correction for rapid repeat measurements of water level change in wetlands. *IEEE Transactions on Geoscience and Remote Sensing*, *60*, 1–15. https://doi.org/10.1109/TGRS.2021.3108751

Onn, F., & Zebker, H. (2006). Correction for interferometric synthetic aperture radar atmospheric phase artifacts using time series of zenith wet delay observations from a GPS network. *Journal of Geophysical Research*, *111*(B9). https://doi.org/10.1029/2005jb004012

Pierdicca, N., Pulvirenti, L., & Chini, M. (2013). Dealing with flood mapping using SAR data in the presence of wind or heavy precipitation. In C. Notarnicola, S. Paloscia, & N. Pierdicca (Eds.), *SAR image analysis, modeling, and techniques XIII* (Vol. 8891, p. 88910K). SPIE. https://doi.org/10.1117/12.2030105

Rosen, P. A., Gurrola, E., Sacco, G. F., & Zebker, H. (2012). The InSAR scientific computing environment. In *EUSAR 2012; 9th European Conference on Synthetic Aperture Radar* (pp. 730–733). VDE.

Wdowinski, S., Hong, S.-H., & Kim, S.-W. (2008a). Evaluation of TerraSAR-X observations for wetland InSAR application. In *2008 IEEE international geoscience and remote sensing symposium (IGARSS)* (Vol. 4, pp. IV1233–IV1236). IEEE. https://doi.org/10.1109/IGARSS.2008.4779952

Wdowinski, S., Kim, S.-W., Amelung, F., Dixon, T. H., Miralles-Wilhelm, F., & Sonenshein, R. (2008b). Space-based detection of wetlands' surface water level changes from L-band SAR interferometry. *Remote Sensing of Environment*, *112*(3), 681–696. https://doi.org/10.1016/j.rse.2007.06.008

Yu, C., Li, Z., & Penna, N. T. (2018a). Interferometric synthetic aperture radar atmospheric correction using a GPS-based iterative tropospheric decomposition model. *Remote Sensing of Environment*, *204*, 109–121. https://doi.org/10.1016/j.rse.2017.10.038

Yu, C., Li, Z., Penna, N. T., & Crippa, P. (2018b). Generic atmospheric correction model for interferometric synthetic aperture radar observations. *Journal of Geophysical Research: Solid Earth*, *123*(10), 9202–9222. https://doi.org/10.1029/2017JB015305

Yu, C., Penna, N. T., & Li, Z. (2017). Generation of real-time mode high-resolution water vapor fields from GPS observations. *Journal of Geophysical Research: Atmospheres*, *122*(3), 2008–2025. https://doi.org/10.1002/2016JD025753

Yunjun, Z., Fattahi, H., & Amelung, F. (2019). Small baseline InSAR time series analysis: Unwrapping error correction and noise reduction. *Computers & Geosciences*, *133*, 104331. https://doi.org/10.1016/j.cageo.2019.104331

Zhang, X., Jones, C. E., Oliver-Cabrera, T., Simard, M., & Fagherazzi, S. (2022). Using rapid repeat SAR interferometry to improve hydrodynamic models of flood propagation in coastal wetlands. *Advances in Water Resources*, *159*, 104088. https://doi.org/10.1016/j.advwatres.2021.104088

Zhang, Y., Li, W., Sun, G., & King, J. S. (2019). Coastal wetland resilience to climate variability: A hydrologic perspective. *Journal of Hydrology*, *568*, 275–284. https://doi.org/10.1016/j.jhydrol.2018.10.048

Zhu, K., Zhang, X., Sun, Q., Wang, H., & Hu, J. (2022). Characterizing spatiotemporal patterns of land deformation in the Santa Ana basin, Los Angeles, from InSAR time series and independent component analysis. *Remote Sensing*, *14*(11), 2624. https://doi.org/10.3390/rs14112624